THESIS

GROWTH AND CHARACTERIZATION OF ULTRA-LOW DAMPING $Co_{25}Fe_{75}$ THIN FILMS

Submitted by

Mitchell Swyt

Department of Physics

In partial fulfillment of the requirements

For the Degree of Master of Science

Colorado State University

Fort Collins, Colorado

Fall 2020

Master's Committee:

Advisor: Kristen Buchanan

Kate Ross
Carmen Menoni

ABSTRACT

GROWTH AND CHARACTERIZATION OF ULTRA-LOW DAMPING $Co_{25}Fe_{75}$ THIN FILMS

This thesis focuses on the growth and characterization of ultra-low damping $Co_{25}Fe_{75}$ thin films. Ultra-low damping in a metal is of interest for the design of new spintronic devices because this offers the opportunity to move both electrons and spin waves over appreciable distances. In this work, the effects of seed and capping layers on the damping parameter and magnetization are investigated. A series of thin films were deposited using DC magnetron sputtering. A combination of X-ray reflectometry (XRR), vibrating sample magnetometry (VSM), and ferromagnetic resonance spectroscopy (FMR) were used to determine the film quality, saturation magnetization, and damping parameters of each film. The results show that the Ta seed layers promoted smooth film growth for $Co_{25}Fe_{75}$, but direct interfaces with Ta or Pt resulting in enhanced damping. Cu spacer layers can be used to disrupt the enhancement but promote rough film growth for the studied sample growth conditions. Damping values in agreement with published results were achieved for two films from the set, with $\alpha = 0.0064 \pm 0.0004$ for Ta/$Co_{25}Fe_{75}$ and $\alpha = 0.0063 \pm 0.0011$ for Ta/Cu/$Co_{25}Fe_{75}$/Cu/Ta.

ACKNOWLEDGEMENTS

There are many people in my life that deserve recognition for the part they played in keeping me on the path to the completion of this work. I would like to acknowledge my advisor, Kristen Buchanan, for giving me the opportunity to be a part of this research. Being able to step into the lab from the moment I arrived at CSU allowed me to explore the world of research and find my passion for it. I want to thank my fellow groupmates, Katie and David, as well as all other past and present members, for welcoming me into the group and helping me to find my feet in the lab.

I would also like to acknowledge amazing fiancée, Alyx. Without her constant support, and baked treats, I would not be where or who I am today. Lastly, my furry friends, Frank, Indy, and Pirate Steve, all deserve special recognition for the quiet support and companionship that pets give.

TABLE OF CONTENTS

CHAPTER 1

INTRODUCTION

1.1. Motivation

Ferromagnetic materials have become a mainstay in everyday life, especially since the advent of information technologies. The storage of information has been a dominated by these materials, in which the state of the magnetic domains has served as the repository of information. From hard disc drives (HDDs) to the magnetic stripe on the back of credit cards, the use of these materials has become ubiquitous. Now, devices exploiting the spin degree of freedom of electrons have been attracting a great deal of research interest. Examples of these devices include magnetic RAM (MRAM)[1–3], spin-torque oscillators (STOs)[4–6], and spin-transfer-torque magnetic random-access memory (STT-MRAM)[7–9]. The magnetic properties of the materials used in these applications need to be fundamentally well understood in order to properly engineer them. The dynamic properties of these materials are especially critical, as they dictate the limits of operating parameters. In particular, there have been extensive searches for low magnetic damping materials, as the damping parameter is crucial for determining working parameters such as energy consumption.

Metallic ferromagnetic thin film materials with low damping are ideally suited for application in devices that require conducting materials. As such, the investigation of the properties of these thin films is an ongoing effort. While bulk ferromagnetic materials have been extensively studied, the increased importance of interfacial effects on the properties thin films necessitates a new look. Recent publications have demonstrated ultra-low damping in $Co_{25}Fe_{75}$ thin films, with the intrinsic damping parameter on the order of 10^{-4} [10,11]. This material, with

a damping parameter comparable the insulating ferrimagnet yttrium iron garnet (YIG), has garnered significant attention as a basis for spintronics applications. Typically, metals have a much higher damping parameter than insulators due to magnon-electron scattering off of conduction band electrons that are not present in insulators. Thus, a metal with a damping parameter comparable to YIG is of interest.

1.2. Objectives

This thesis will focus on the verification of ultra-low damping measurements in $Co_{25}Fe_{75}$ thin films, as well as investigate the effects of varying seed and capping layers on the Gilbert damping. Several sample designs will be investigated, with their effects on the magnetic properties of the $Co_{25}Fe_{75}$ measured: x-ray reflectometry will be used to calibrate deposition rates and examine film quality, vibrating sample magnetometry will be used to measure the saturation magnetization, and ferromagnetic resonance spectroscopy will be used to measure the damping in each film.

1.3.Outline

This thesis will be structured according to the following:

Chapter 2 will review the necessary background information to understand magnetism in materials, phenomenological damping, and ferromagnetic resonance. The origin of magnetism in materials will be discussed, as well as the interactions between fundamental sources of magnetism. The semi-classical approach of effective The semi-classical approach will be used to understand the macroscopic effects of microscopic interactions. The equations of motion will be used to describe the time-evolution of the magnetization, and the phenomenological damping parameter will also be described. Resonance conditions, and resonance linewidths, for a

ferromagnetic material will be derived an effective field approach, as well as the equations of motion for the magnetization.

Chapter 3 will provide a review of the experimental techniques used in this work. The instrumentation will be briefly described. The deposition technique, DC magnetron sputtering, will be discussed, as well as the techniques used to measure the film quality (x-ray reflectometry), magnetic moment (vibrating sample magnetometry), and damping (ferromagnetic resonance spectroscopy).

Chapter 4 will present the results of measurements undertaken in this work. It will also present a discussion of the results and a comparison of the results with previous results from the literature for $Co_{25}Fe_{75}$. The saturation magnetization (M_S), the in-plane uniaxial anisotropy energy density (K), and the Gilbert damping parameter (α), will be summarized for each of the thin film samples. The influence of sample design, as well as measurement techniques, on these parameters are discussed.

CHAPTER 2

BACKGROUND INFORMATION

2.1. Origin of Magnetism

Understanding magnetism in materials requires the understanding of the fundamental mechanism of how magnetic moments interact. At the most fundamental level, these moments arise from the quantum mechanical particle spin and orbital angular momentum. By understanding the interactions that drive the dynamics of magnetic materials, the dynamics can be used to extract important material information.

As the origin of magnetism in materials is inherently quantum mechanical, so too are the interactions between moments. A semiclassical approach will be used here in order to represent the interactions in a form that is more useful for analyzing experimental ferromagnetic resonance measurement. Effective fields are used at a macroscopic level to represent the effects of interactions between moments. Fields are used instead of the quantum mechanical operators, allowing for the application of methods from the study of classical electromagnetism.

The interactions between magnetic moments from several different effects must be considered. The dipolar interaction describes the interaction of one moment with the dipolar field originating from another. The energy describing this interaction, between two dipole moments $\boldsymbol{m}_1$ and $\boldsymbol{m}_2$, is given in [12] as

$$E_{dip-dip} = -\frac{\mu_0}{4\pi|\boldsymbol{r}|^3}\left[3(\boldsymbol{m}_1 \cdot \hat{\boldsymbol{r}})(\boldsymbol{m}_2 \cdot \hat{\boldsymbol{r}}) - \boldsymbol{m}_1 \cdot \boldsymbol{m}_2 + \frac{8\pi}{3}\boldsymbol{m}_1 \cdot \boldsymbol{m}_2 \delta(\boldsymbol{r})\right] \tag{2.1}$$

where $\hat{\boldsymbol{r}}$ is the unit vector pointing from one moment to the other, μ_0 is the permeability of free space, and $\delta(\boldsymbol{r})$ is the Dirac delta function. The total dipole-dipole interaction density requires a summation over the interaction between every moment in the media with every other moment in

the media. To replace the summation with a continuous field, the dipole interaction potential is found using a Green's function approach, derived from the requirement that there be no magnetic monopoles, $\nabla \cdot \boldsymbol{B} = \mu_0 \nabla \cdot (\boldsymbol{H} + \boldsymbol{M}) = 0$, from [12],

$$\mathrm{E}_{\mathrm{dip-dip}}(\boldsymbol{r}) = \int d\boldsymbol{r}' \left(\frac{\boldsymbol{r} - \boldsymbol{r}'}{4\pi |\boldsymbol{r} - \boldsymbol{r}'|} \right) \cdot \boldsymbol{M}(\boldsymbol{r}') \tag{2.2}$$

The demagnetization field, $\boldsymbol{H}_{demag}$, is found simply by taking the negative gradient of the potential,

$$\boldsymbol{H}_{demag} = -\nabla \mathrm{E}_{dip-dip} \tag{2.3}$$

$\boldsymbol{H}_{demag}$ becomes dependent on the external field and points in the opposite direction of the magnetization, hence the term demagnetizing. For uniform external fields, the demagnetization field can be written as

$$\boldsymbol{H}_{demag} = \begin{bmatrix} -N_x M_x \\ -N_y M_y \\ -N_z M_z \end{bmatrix} \tag{2.4}$$

where it is required that $N_x + N_y + N_z = 1$ (this is the requirement in SI units, in CGS units $N_x + N_y + N_z = 4\pi$). These are known as the demagnetization factors and are dependent on the shape of the media. They are scalar quantities. For certain geometries, they have simple, tabulated solutions.

The exchange interaction is a consequence of the antisymmetric nature of fermions, in that they cannot exist in the same state. By enforcing this condition on adjacent spins in a material, the exchange energy is given by

$$E_{exchange} = -2J \sum_{i=1}^{N} \boldsymbol{S}_i \cdot \boldsymbol{S}_{i+1} \tag{2.5}$$

Where J is the exchange integral, while $\boldsymbol{S}_i$ and $\boldsymbol{S}_{i+1}$ are the spin operators for neighboring atoms. (2.5) gives the energy from an atomistic point of view, where it is necessary to sum over the spins of every discrete atom. The sign of J dictates whether adjacent spins will be aligned or anti-aligned, distinguishing ferromagnets ($J > 0$) and antiferromagnets ($J < 0$). Moving to a continuum model, the effective exchange field is given by

$$\boldsymbol{H}_{ex} = \lambda_{ex} \nabla^2 \boldsymbol{M} \tag{2.6}$$

where $\lambda_{ex} = \sqrt{\frac{A}{2\pi M_S^2}}$ is the exchange length. A is the exchange parameter, and M_s is the saturation magnetization.

Magnetic anisotropy occurs when the energy of the magnetic system is no longer independent of the direction of magnetization. It arises from several sources, including symmetry of the crystal lattice, interfacial effects such as spin-orbit coupling between layers, as well as the shape of the system. In systems with uniaxial anisotropy, with energy given by [13]

$$E_{an} = K_u sin^2\theta \tag{2.7}$$

where V is the volume of the system, K_u is the uniaxial anisotropy constant, and θ is the angle of the magnetization from the anisotropy axis, the energy is minimized when the magnetization lies along the axis of anisotropy. The anisotropy field is given by

$$\boldsymbol{H}_{an} = -\frac{1}{M} \nabla_M E_{an} \tag{2.8}$$

where ∇_M is the gradient with respect to the components of the magnetization.

Other magnetic interactions, such as the Dzyaloshinskii-Moriya interaction (DMI), a spin superexchange interaction in which two spins' interaction is mediated by an adjacent atom, can also be modeled with effective fields [14,15].

2.2. Equations of Motion

Equations of motion form the base from which to approach dynamic systems. They serve as a framework from which different properties can be understood, from the resonance conditions of ferromagnetic materials under an applied field, to the motion of magnetic structures such as magnetic domains [16] or skyrmions [17]. There are several approaches to modeling magnetization dynamics, each applicable to different scenarios and constraints; the three approaches discussed here are especially applicable in the study of magnetic damping and ferromagnetic resonance.

The simplest equation of motion for a magnetic system under an applied field comes in the form of the torque equation,

$$\frac{\partial \boldsymbol{M}}{\partial t} = -|\gamma| \boldsymbol{M} \times \boldsymbol{H}_{eff} \tag{2.9}$$

where $\boldsymbol{H}_{eff} = \boldsymbol{H}_{ext} + \boldsymbol{H}_{demag} + \boldsymbol{H}_{\boldsymbol{an}} + \cdots$. This equation lacks any term to damp the rotation of the magnetization but can be used to derive resonance conditions for systems with different effective field conditions, which will be explored later.

Real systems have intrinsic sources of damping, that are not adequately captured by the torque equation alone. Without finding a way to introduce damping into the equations of motion, the magnetization has no method of relaxation included in the equation of motion. Two approaches are commonly used to insert a phenomenological damping into the equation of motion. A third approach inserts two separate relaxation rates into the equation of motion.

The first approach was developed by Landau and Lifshitz [18],

$$\frac{\partial \boldsymbol{M}}{\partial t} = -|\gamma| \boldsymbol{M} \times \boldsymbol{H}_{eff} + |\gamma| \frac{\lambda}{M_s^2} \boldsymbol{M} \times (\boldsymbol{M} \times \boldsymbol{H}_{eff}) \tag{2.10}$$

where the dimensionless damping parameter is λ. The damping torque lies in the plane perpendicular to the effective field. In this approach, the damping preserves the component of the magnetization that lies parallel to the effective field. The second approach was later proposed by Gilbert [19]

$$\frac{\partial \boldsymbol{M}}{\partial t} = -|\gamma|\boldsymbol{M} \times \boldsymbol{H}_{eff} + \frac{\alpha}{M_s}(\boldsymbol{M} \times \frac{\partial \boldsymbol{M}}{\partial t}) \tag{2.11}$$

where α is the dimensionless damping parameter. The damping torque points from the magnetization vector to the effective field. This model preserves the total magnetic moment, allowing the z component to be dynamic. It can be shown that in the limit of low damping, both approaches reduce to the same equation, leaving the choice of which approach to use a matter of convenience. Often the choice revolves around whether the time derivative of the magnetization is easily written.

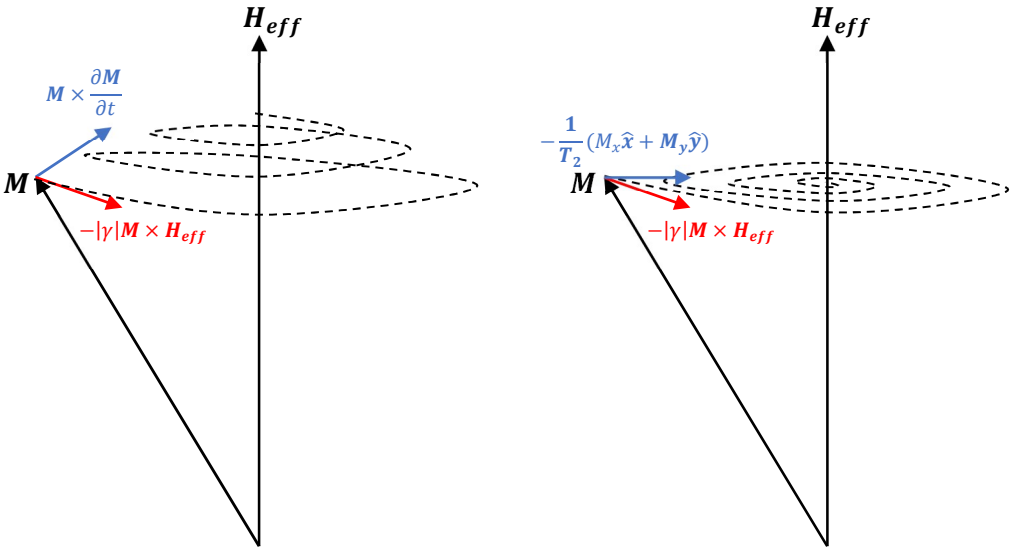

Figure 2.1: Cartoons depicting the directions of the terms in the Landau-Lifshitz (LL) and Landau-Lifshitz-Gilbert (LLG) equations on the left, with the Bloch equation on the right. The damping term in the LL/LLG equations points perpendicularly from the magnetization vector, thus preserving the magnitude of the magnetization vector. The damping in the Bloch equation points in the plane perpendicular to the saturation direction, preserving the component of the magnetization parallel to the effective field. Trajectories of the rotating magnetization are sketched in dotted lines.

The third approach was introduced by Bloch [20],

$$\frac{\partial \boldsymbol{M}}{\partial t} = -|\gamma|\mathbf{M} \times \mathbf{H}_{\text{eff}} - \frac{1}{\mathrm{T}_2}\left(M_x\hat{x} + M_y\hat{y}\right) - \frac{1}{T_1}(M_z - M_s)\hat{z}$$

where the relaxation times, T_1 and T_2, have been introduced. For small deviations from the equilibrium direction, which is to say that $M_z \approx M_s$, the last term effectively vanishes. Doing so preserves the length of the $\hat{z}$-component of the magnetization, causing the relaxation to occur in the plane perpendicular to the saturation direction.

2.3. Phenomenological Damping

The phenomenological damping inserted into the equations of motion serve as a catch-all to describe the effect of the variety of pathways a magnetic system can take to relax. Sources of damping can be both intrinsic and extrinsic to the system; contributions to damping can come from magnon-electron scattering, ion impurity scattering, two-magnon scattering, or a variety of other pathways. The intrinsic damping is a material property, constant for any sample made of the same material [21,22] Extrinsic sources arise from the construction of the sample, whether that be from impurities or other inhomogeneities, such as roughness at the surface or interfaces within the sample.

The primary extrinsic mechanism for relaxation in ultrathin films come from surface-defect-induced two-magnon scattering [23–25]. In ultrathin films, the dispersion curve for magnons has degeneracy with the uniform mode, allowing for defects in the surface or bulk to promote scattering from the uniform mode into the degenerate spin wave modes. To conserve angular momentum, the uniform mode must scatter into two magnons with opposite wave vectors. This process is seen alongside inhomogeneous broadening, seen in ferromagnetic resonance measurements, due to defects in films promoting both processes [26]. Spin pumping

into adjacent layers in multilayer structures, as well as contributions from the magnetic proximity effect, are other important sources of damping [27].

2.4. Ferromagnetic Resonance

Let us now apply the equations of motion discussed to a magnetic system. Consider the case of a ferromagnet saturated in a single domain state by an applied field. The applied field will cause the spins in the ferromagnet to precess about it. Unlike a free electron, the frequency at which the spins will precess about the field depends not only on the applied field, but also on the other contributions arising from the ferromagnet itself, such as the demagnetization field that is due to the shape of the ferromagnet, and the anisotropy field. Exchange fields provide a wavevector-dependent contribution to the frequency, thus having no impact on the uniform mode. The uniform, in-phase precession of all spins in the ferromagnet is known as the ferromagnetic resonance. In order to determine the resonant frequency, let us examine a typical scenario more closely. A diagram of the system can be found in Fig. 2.2.

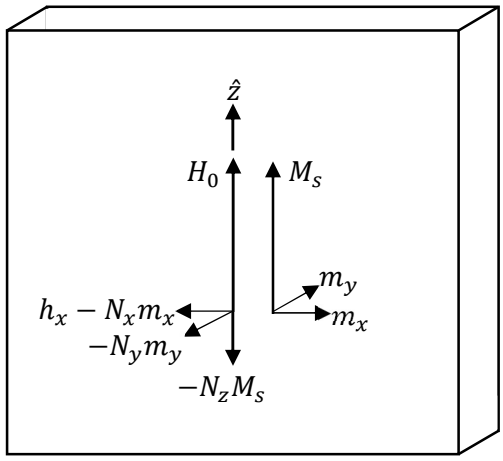

Figure 2.2: Diagram of the fields and magnetization of a ferromagnetic sample under applied field. Vector components of the magnetization and effective field are shown. The sample is saturated along the *z*-axis, with the dynamic components of both the magnetic field and magnetization lying in the *xy* plane. The microwave field h_x lies along the *x*-axis.

The fields are applied such that

$$\boldsymbol{H_{ext}} = H_0\hat{z}, \boldsymbol{h_{micro}} = h_x\hat{x}. \tag{2.12}$$

The sample will be magnetized such that the static magnetization will be along the $\hat{z}$ direction, with dynamic components along the other axes, allowing us to write

$$\boldsymbol{M} = \boldsymbol{M_z} + \boldsymbol{m}(t), |\boldsymbol{M_z}| \cong M_s, |\boldsymbol{m}| \ll M_s \tag{2.13}$$

where we have assumed that the dynamic components of the magnetization are sufficiently small that the static magnetization is equivalent to the saturation magnetization. Lower case symbols are chosen to represent dynamic components. This is a special case, in which we have assumed that $\boldsymbol{H}_{ext}$ lies along the axis of anisotropy, which causes the magnetization to align to $\boldsymbol{H}_{ext}$. A more general treatment that uses an energy approach that fully incorporates anisotropy effects can be found in [28]. The sample shape dependent demagnetization factors, (N_x, N_y, N_z), will contribute an effective field of

$$\boldsymbol{H_{demag}} = \begin{bmatrix} -N_x m_x \\ -N_y m_y \\ -N_z M_z \end{bmatrix} \tag{2.14}$$

The total effective field in the sample can hence be written as,

$$\boldsymbol{H_{eff}} = \begin{bmatrix} h_x - N_x m_x \\ -N_y m_y \\ H_0 - N_z M_s \end{bmatrix} \tag{2.15}$$

We have neglected the exchange field, as its contribution to the dispersion relation vanishes in the case of the uniform mode (ferromagnetic resonance). It is important, however, for properly understanding spin wave dispersion. The precession of the spins about the field will be governed by the torque equation,

$$\frac{d\boldsymbol{M}}{dt} = -|\gamma|\boldsymbol{M} \times \boldsymbol{H_{eff}} \tag{2.16}$$

where γ is the gyromagnetic ratio. Substituting (2.15) into (2.16) gives,

$$\frac{dm_x}{dt} = -|\gamma|[H_0 + (N_y - N_z)M_s]m_y \tag{2.17a}$$

$$\frac{dm_y}{dt} = -|\gamma|[M_s h_x - (N_x - N_z)m_x M_s - m_x H_0] \tag{2.17b}$$

$$\frac{dM_z}{dt} \cong 0 \tag{2.17c}$$

In (2.17c), we have neglected the product of small quantities, the dynamic components of the magnetization and h_x. Assuming a complex exponential time dependence, $\boldsymbol{M} \propto \exp(i\omega t)$, these equations give a resonance condition of,

$$\omega = |\gamma|\sqrt{[H_0 + (N_y - N_z)M_s][H_0 + (N_x - N_z)M_s]} \tag{2.18}$$

Of particular interest for this work, the special case of a plane sample with uniaxial anisotropy gives a resonance condition of,

$$\omega = |\gamma|\sqrt{[H_0 + 4\pi M_s + \frac{2K}{M_s}][H_0 + \frac{2K}{M_s}]} \tag{2.19}$$

(2.18-19) are often referred to as the Kittel equations.

2.5. Power Absorption and Resonance Linewidth

Of particular interest for experiment is the resonance linewidth. The linewidth is a tool to extract the effective damping parameter. As shown previously, the Kittel equations, (2.18-19), provide the resonance frequency; we will now include the damping to determine the linewidth of the resonance.

A microwave field applied perpendicular to the saturation direction will do work on the magnetization of the sample, allowing us to write the power absorbed by the sample as,

$$P_a = \frac{dW}{dt} = \boldsymbol{h}(t) \cdot \frac{d\boldsymbol{m}(t)}{dt} \tag{2.20}$$

We assume that the microwave field and dynamic magnetization can be written as,

$$\boldsymbol{h}(t) = Re\left[\boldsymbol{h}_0 e^{i\omega t}\right] = \frac{1}{2}\left[\boldsymbol{h}_0 e^{i\omega t} + \boldsymbol{h}_0^* e^{-i\omega t}\right] \tag{2.21a}$$

$$\boldsymbol{m}(t) = Re\left[\boldsymbol{m}_0 e^{i\omega t}\right] = \frac{1}{2}\left[\boldsymbol{m}_0 e^{i\omega t} + \boldsymbol{m}_0^* e^{-i\omega}\ \right]. \tag{2.21b}$$

This form of the microwave field, $\boldsymbol{h}(t)$, matches that for a microwave cavity, strip-line, or shorted waveguide. Plugging (2.21a-b) into (2.20) and dropping the time dependence, as we are only interested in the power absorbed, gives

$$P_a = -\tfrac{1}{2}\omega(\boldsymbol{h}_0^* \cdot \boldsymbol{m}_0). \tag{2.22}$$

Writing $\boldsymbol{m}$ as a product of $\boldsymbol{h}$ and the magnetic susceptibility tensor gives,

$$P_a = -\frac{1}{2}\omega|\boldsymbol{h}_0|^2(\mathrm{X}_{11}) \tag{2.23}$$

where X_{11} is a component of the magnetic susceptibility tensor. In this step we have assumed that we are in the linear response regime. We are then left to find X_{11}, defined by $X_{11} = m_x/h_x$.

As we are now interested in the damping as well as the resonant frequency, we use the Landau-Lifshitz-Gilbert equation, (2.11), to model the dynamics of the system. The additional term, as compared to the torque equation, is a phenomenological description of the damping. Inserting $\boldsymbol{M}$ and $\boldsymbol{H_{eff}}$ into (2.11) gives a system of equations,

$$i\omega m_x = -|\gamma|\left[H_0 + \left(N_y - N_z\right)M_s\right]m_y - i\omega\alpha m_y \tag{2.24a}$$

$$i\omega m_y = -|\gamma|[M_s h_x - (N_x - N_z)m_x M_s - m_x H_0] + i\omega\alpha m_x \tag{2.24b}$$

For simplicity, we define,

$$\omega_x = |\gamma|\left[H_0 + \left(N_y - N_z\right)M_s\right] \tag{2.25a}$$

$$\omega_y = |\gamma|[H_0 + (N_x - N_z)M_s] \tag{2.25b}$$

Thus,

$$i\omega m_x = -\omega_y - i\omega\alpha m_y \tag{2.26a}$$

$$i\omega m_y = \omega_x m_x - |\gamma|M_s h_x + i\omega\alpha m_x \tag{2.26b}$$

Solving for m_x allows us to arrive at X_{11},

$$X_{11} = \frac{|\gamma|M_s(i\omega\alpha + \omega_y)}{-\omega^2 - \omega^2\alpha^2 + \omega_x\omega_y + i\omega\alpha(\omega_x + \omega_y)} \tag{2.27}$$

In the limit of low damping, $\alpha^2 \ll 1$. We drop the $-\omega^2\alpha^2$ term in the denominator. Rearranging, we obtain

$$X_{11} = \frac{\omega_M}{4\pi}\frac{[\omega_x\omega_y^2 - \omega^2\omega_y + \omega^2\alpha^2(\omega_x + \omega_y)] - i\alpha\omega(\omega^2 + \omega_y^2)}{(\omega_x\omega_y - \omega^2)^2 + \omega^2\alpha^2(\omega_x + \omega_y)^2}. \tag{2.28}$$

where $\omega_M = 4\pi|\gamma|M_s$. Inserting (2.28) into (2.23)

$$P_a = \frac{1}{2}\alpha\omega^2|\boldsymbol{h}_0|^2\frac{\omega_M}{4\pi}\frac{(\omega^2 + \omega_y^2)}{(\omega_x\omega_y - \omega^2)^2 + \alpha^2\omega^2(\omega_x + \omega_y)^2}. \tag{2.29}$$

This equation can be used to fit an FMR power absorption profile. Typically lock-in detection techniques are used in practice, however, so the signal appears as the derivative of the power absorption profile. Therefore, the derivative of (2.29) with respect to the applied field, at fixed ω, is used to fit the FMR data in this work. Recall that the applied field appears in both ω_x and ω_y,

The field swept linewidth ΔH, when measured by applying a fixed frequency microwave field and sweeping the static field, can be related to the frequency swept linewidth $\Delta\omega$, that is measured by applying a fixed static field and sweeping the microwave frequency, through

$$\Delta H = \frac{d\omega_{fmr}}{dH}\Delta\omega \tag{2.30}$$

where ω_{FMR} is the resonant frequency given by the Kittel equation, (2.18). Using (2.18) to find the FWHM of power absorption at fixed static field, we find that

$$\Delta\omega = \alpha(\omega_x + \omega_y) \tag{2.31}$$

Once inserted, this gives a final relation

$$\Delta H = \frac{2\alpha}{|\gamma|}\omega_{FMR} \tag{2.32}$$

This equation holds for a system without inhomogeneous broadening, as it predicts a zero linewidth at zero field. As discussed before, extrinsic sources of damping result in a zero-field linewidth, so a constant offset must be added to account for that.

$$\Delta H = \frac{2\alpha}{|\gamma|}\omega_{FMR} + \Delta H_0 \tag{2.33}$$

(2.33) is sufficient to capture that behavior and will be later used to fit experimental linewidth data.

2.6. Conclusion

The necessary framework to discuss ferromagnetic resonance and magnetic relaxation were presented. Several pathways for magnetic systems to relax were discussed, as well as a method for relating the linewidth of the ferromagnetic resonance to the damping parameter. These results are applicable to thin film materials in the linear response regime.

CHAPTER 3

EXPERIMENTAL TECHNIQUES

3.1. Introduction

In this section, the experimental techniques employed in this work will be discussed, from deposition of thin films using DC magnetron sputtering, to the characterization techniques of x-ray reflectometry (XRR), vibrating sample magnetometry (VSM), and ferromagnetic resonance spectrometry (FMR). XRR is used to calibrate deposition rates and evaluate film quality, VSM is used to measure the saturation magnetization of each sample, and FMR is used to evaluate the damping parameters.

3.2. DC Magnetron Sputtering

Physical vapor deposition (PVD) methods have become the preferred set of techniques to grow thin film materials for many applications [29–33]. These techniques use physical processes, such as sputtering or evaporation, to transport material from a target and condense it into a thin film on a substrate [34]. One or more of the PVD techniques can be used to deposit most inorganic materials, and PVD methods produce less waste than chemical vapor deposition techniques [34]. In particular, DC magnetron sputtering has become a mainstay in the deposition of magnetic materials [31,32]. DC magnetron sputtering is an offshoot of traditional DC sputtering that has overcome many of the issues with traditional DC sputtering.

DC sputtering operates under a well understood framework. A general system operates as follows: there is a DC potential bias between the target and the substrate. Vacuum pressures are required to maintain the plasma used to sputter the target, so the substrate and target material are placed in a vacuum chamber. Process gas, in this work Ar, is flowed into the vacuum chamber

and collides with stray electrons accelerated by the bias across the chamber. This collision produces a positive ionized gas, which is then accelerated towards the anode. The ionized gas hits the target and sputters material from the target, which is ejected upwards toward the substrate. This is the general mechanism under which DC sputtering operates to deposit material on a substrate.

DC magnetron sputtering improves upon DC Sputtering by using magnetic fields to increase the efficiency of the plasma generation [34]. An array of permanent magnets, typically NdFeB, is bonded to the sputtering gun under the target. The magnets induce the formation of a confined, toroidal plasma region over the target disc by confining electron motion. In this region, there is increase collision rates of electrons with the process gas due to the increased density of electrons. This enhances the generation of plasma and reduces the process gas pressure required to operate. Forming this region of concentrated electron density allows for the plasma to be sustained at operating pressures of order millitorr. As a consequence of having lower operating pressures, there are reduced gas phase collisions of sputtered material with process gas atoms, which reduces scattering of the sputtered material that would otherwise reduce the amount of sputtered material impinging on the substrate. With reduced scattering, the trajectory of sputtered material is ballistic, and the deposition rates are higher. Similarly, reduced working voltages are required to maintain the same deposition rate as in traditional DC sputtering.

The system used in this work is an AJA Orion 5 sputtering system, fitted with three 3" sputtering guns. A rotary vane pump and a turbomolecular pump are used in tandem to evacuate the vacuum chamber, reaching base pressures as low as 10^{-9} Torr. The deposition occurs at room temperature, and an operating pressure of 5 mTorr Ar is used. Deposition rates are monitored in situ with a crystal rate monitor and precise deposition rates are calculated using XRR

measurements of timed depositions. 50 W DC is delivered to the targets, with typical operating voltages in the 200-400 V range, and operating currents in the range of 100-200 mA.

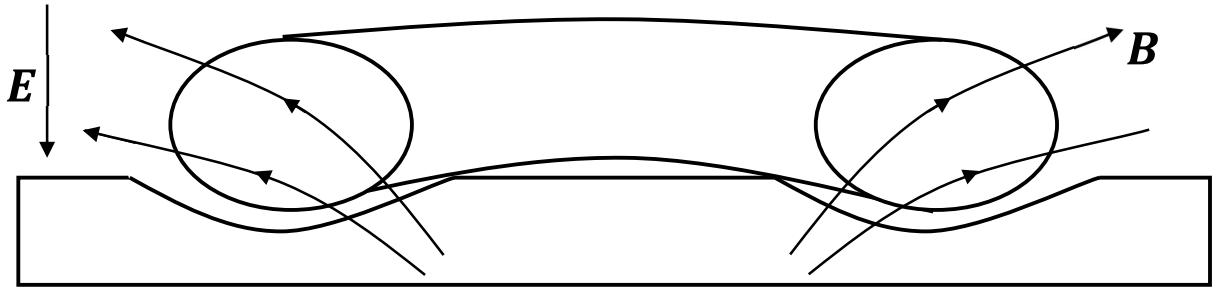

Figure 3.1: The magnetic field from the permanent magnets beneath the target, combined with the electric field, forms a toroidal discharge plasma by confining electron motion. The efficiency of plasma formation is enhanced in this region, allowing for lower operating pressures, of the order single millitorr. The plasma etches a circular racetrack into the target due to the enhanced sputtering in this region.

3.3. X-ray Reflectometry

X-ray reflectometry (XRR) is a characterization technique that uses grazing incidence x-ray light to measure the reflectivity profile of thin, planar materials. First demonstrated experimentally by Parratt [9] through the measurement of copper films deposited on glass, XRR has since served as a routine technique to quantitatively characterize thin films. The reflectivity profiles provide quantitative information on the thickness, density, and roughness of the film, or in the case of multilayers, each layer [35].

The technique centers on measuring deviations from the reflectivity profile predicted by the Fresnel equations for reflection and transmission at plane interfaces of optical media. The deviation of the pattern measured from the pattern predicted by the Fresnel equations gives insight into the physical properties of the sample. Fresnel solutions hold for the reflection of light off a single, planar boundary between two layers [36,37]; the roughness of real interfaces causes a deviation from these solutions through the modification of the optical properties of the interfacial layer [35,37]. By fitting the measured reflectivity to a model, the roughness of the

interface, the thickness of the layers, and the density of the material in each layer can be extracted [37].

To measure the reflectivity profile of very thin films (of order single nanometer), an EM wave source of comparable wavelength is required. The most common x-ray source used, and the one used in this work, is a Cu $K\alpha_1$ line source. The source is held at 40 kV in order to stimulate emission of the 0.1541867-nm wavelength line. A photodetector is used to capture the beam reflected from the sample as the angle of incidence θ is varied, depicted in Figure 3.2. Both the photodetector and the incident beam are scanned in tandem.

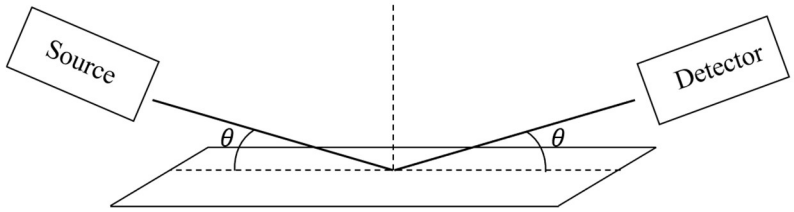

Figure 3.2: Diagram of the XRR experiment. The source produces x-rays that are incident on the sample at grazing angles θ. The reflected light is captured by a detector positioned at the sample angle relative to the sample.

The sample to be analyzed is placed onto the sample mount and centered onto the beam path by hand. A centering routine is then used to maximize the intensity of reflected light. The height of the sample, the position of the sample in the beam path, and the rocking curve are all optimized in the alignment procedure. The alignment procedure has been automated for modern instrumentation to decrease measurement times and to improve the quality of alignment.

During each measurement, the detector and beam source are scanned from $2\theta = 0.2$ to 10 degrees. A short scan was made in order to evaluate the quality of alignment before each measurement. The source is scanned at a rate of 0.35 degrees/min, sufficient to capture the reflectivity profile (about 28 minutes). The collected data takes the form of an intensity profile, showing the intensity of the reflected x-rays versus 2θ. For films of low roughness, the

interference fringes are visible at up to 10 degrees due to the high quality of the interfaces. The fringes arise from x-rays reflecting off interfaces within the sample interfering with incoming x-rays.

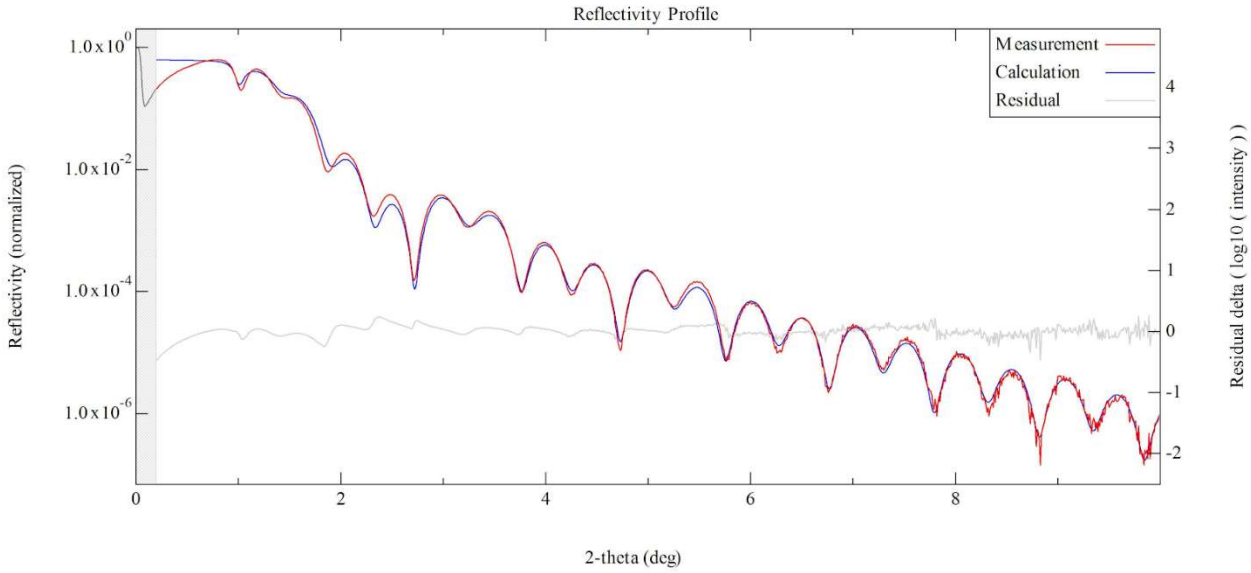

Figure 3.3: X-ray Reflectivity measurement of Si/Ta/$Co_{25}Fe_{75}$/Pt with fit. The film was of high quality, with interface roughness for each layer in the range 0.2-0.65 nm, allowing for clear fringes up to 10 degrees.

To analyze the collected intensity profile, a model of the sample is constructed to provide a starting point for the fitting procedure. It consists of each layer of the sample, including the substrate, and their properties, such as density and approximate thickness. The model is then fit to the data using a genetic algorithm, which has been shown to effectively find the global minimum for this problem without getting stuck in a local minima [38]. Material density, layer thickness, and interface roughness are used as free parameters in this minimization.

3.4. Vibrating Sample Magnetometry

Vibrating Sample Magnetometry (VSM) is a technique that is used to measure the magnetic moment of a sample by measuring a current induced in pick-up coils by the stray field

from an oscillating sample. The sample is magnetized by an applied field from an electromagnet [39]. As the stray field emerging from a magnetic sample is proportional to the magnetic moment of the sample, the induced current provides quantitative information on the magnetization of the sample. The design of the VSM itself is sufficiently simple that the original instrument was constructed with parts found in a campus cafeteria [40]. Modern instrumentation allows for sensitivity to moments of order 10^{-7} emu [41]. VSM serves as a routine technique for rapidly characterizing magnetic samples, due to its short data collection times and ease of use.

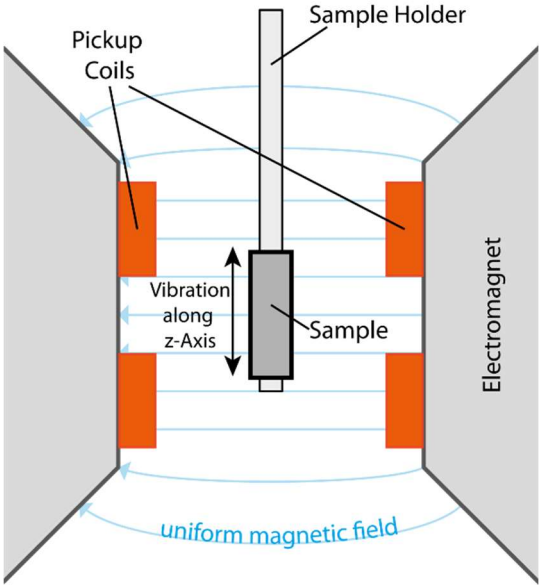

Figure 3.4: Schematic diagram of VSM.

The sample to be measured is mounted onto a rod, typically made of quartz or Pyrex, which is attached to a vibrating drumhead. The sample is centered between the pickup coils. A static field is applied by an electromagnet. The sample is vibrated by the drumhead, typically at 40 Hz. The flux from the stray field of the sample through the pickup coils induces a voltage in the coils due to Faraday's Law of Induction, proportional to the magnetic moment of the sample. The instrument is calibrated through the use of a standard sample of known magnetic moment, allowing for quantitative measurements of magnetic moments.

Hysteresis loops are measured by sweeping the magnetic field and measuring the moment at each field position. In order to remove signal contributions from the rod, substrate, or even dust adhered to the tape used to attach the sample, an additional measurement is taken along the same field loop with a reference piece of substrate, taken from the same wafer as the sample. An example of a background measurement can be found in the inset of Figure 3.5. It is important that the reference be from the same wafer, as it will have to closest impurity profile and signal as the substrate from the measured sample. For very thin or weakly magnetic films it is important to correct for this signal, as it can be on the same order of magnitude as the signal from the sample [42].

The signal from the sample is extracted from the total signal, such as in Figure 3.5, according to (3.1),

$$\boldsymbol{S}_{mag} = \frac{1}{V_{mag}}\left(\boldsymbol{S}_{tot} - \frac{A_{sample}}{A_{ref}}\boldsymbol{S}_{ref}\right) \tag{3.1}$$

where $\boldsymbol{S}_{mag}$ is the signal from the magnetic layer of the sample, V_{mag} is the volume of the magnetic layer of the sample, $\boldsymbol{S}_{tot}$ is the total measured signal, $\boldsymbol{S}_{ref}$ is the reference measurement made with the bare piece of substrate, A_{sample}, A_{ref} are the respective areas of the substrates for the sample and reference substrate. The reference measurement is scaled by the ratio of the substrate areas in order to proportionately subtract out the substrate signal.

Once the magnetic signal is extracted, linear regression on the saturated portions of the sample is performed. The *y*-intercept is then used to calculate M_s, as any slope in this portion is caused by diamagnetic, or paramagnetic, responses. This slope is typically very small, resulting in only a minor correction. Each of these responses scales linearly with the applied field, allowing for the linear regression to adequately capture their contribution.

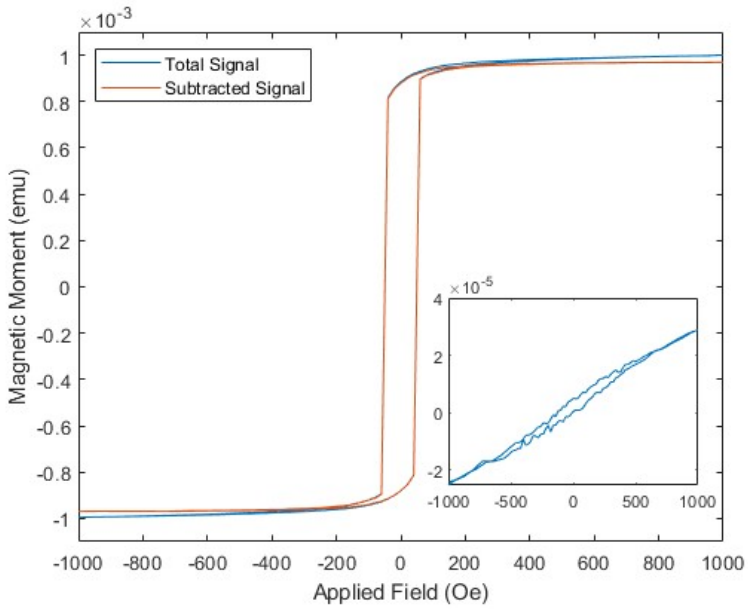

Figure 3.5: Hysteresis measurements for 20 nm of $Co_{25}Fe_{75}$ on Si, showing $\boldsymbol{S}_{mag} * V_{mag}$. Deposited at 5 mTorr, the sample is uncapped, and has a natural oxide layer formed on top. The raw and background-corrected magnetic signals, from (3.1), are in the main plot. The reference signal, from a piece of the same Si wafer and the sample rod, is plotted in the inset with the axes corresponding to the main plot. Notice the reference signal is 2 orders of magnitude smaller than the total signal.

3.5. Ferromagnetic Resonance

Ferromagnetic Resonance Spectroscopy (FMR) is a workhorse technique routinely used to characterize ferromagnetic materials. First used experimentally by Griffiths [43], the technique has become the method of choice to measure a variety of magnetic properties in materials. FMR can characterize a variety of properties, including the product of the saturation magnetization and gyromagnetic ratio, the magnitude and direction of the magnetic anisotropy [44], the exchange coupling in multilayer systems [45,46], and the Gilbert damping parameter [23,47]. Typically, FMR measures the ferromagnetic resonance, discussed before, by sweeping the applied field at a fixed frequency, though the reverse can also be done.

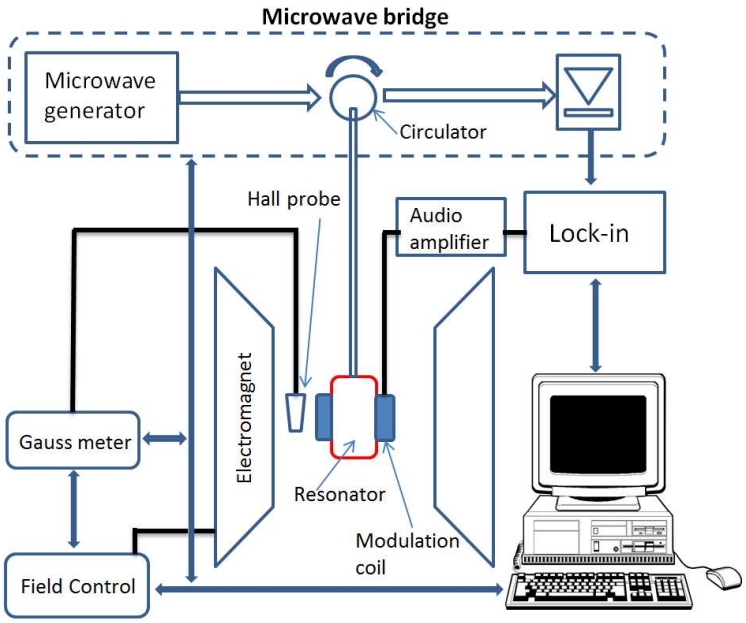

Figure 3.6: Schematic diagram of shorted waveguide FMR. The electromagnet provides the applied field, while the microwave generator provides the fixed frequency microwave field. The microwave bridge sends the microwave signal to the sample, the reflected signal to the detector, and protects the microwave generator from the reflected power [48].

A schematic diagram of an FMR apparatus can be seen in Figure 3.6. The resonator used can be either a shorted waveguide, or a cavity. The shorted waveguide allows for a band of frequencies to be used, while the cavities allow for higher sensitivity at a single, well known frequency. In this work, a shorted waveguide, Ku band (approximately 12-18 GHz), was used for each measurement. During a typical measurement, a sample is placed at the end of a shorted waveguide. An external field is applied in the plane of the sample, while a fixed frequency microwave signal is sent from a microwave signal generator to the sample mounted at the end of a shorted waveguide. The mode supported by the waveguide has the magnetic field oscillating in the plane of the sample, orthogonal to the applied field from the electromagnet. The oscillating field drives the precession of the magnetization of the sample. The applied field is swept through the resonance, while the corresponding drop in power reflected from the sample is monitored. The power absorbed by the sample can be quite small, due to the low volume of magnetic

material in thin films, so lock-in detection techniques are used in order to increase sensitivity. To this end, a small field oscillation, parallel to the applied field, is applied by modulation coils.

Due to the use of lock-in detection techniques, the signal appears as the derivative of the power reflected with respect to the applied field. Thus, the signal appears as the derivative of a Lorentzian. The signal is then fit in order to extract the linewidth and resonant field. When more than one magnetic layer is present, as in the case of multilayers, multiple signals will appear due the different resonant conditions for each layer and due to coupled modes. Each signal can be fit individually to extract the linewidth and resonant field for the corresponding layer.

The experimental FMR linewidth data is fit to

$$H_{pp} = \Delta H_0 + \frac{4\pi\alpha_{eff}}{|\gamma|} f \tag{3.2}$$

where H_{pp} is the resonant field swept linewidth, ΔH_0 is the inhomogeneous line broadening, α_{eff} is the effective Gilbert damping parameter, $\frac{|\gamma|}{2\pi} = 2.8\ MHz/Oe$ is the gyromagnetic ratio, and f is the resonant frequency. This is the same as (2.33), but with the angular frequency, ω_{fmr}, exchanged for $2\pi f$. The effective Gilbert damping is a phenomenological parameter that includes all sources of damping, both intrinsic and extrinsic. The resonant field data can be fit to the Kittel equations for different anisotropy conditions, such as (2.18-2.19), in order to extract information about the anisotropy energy density.

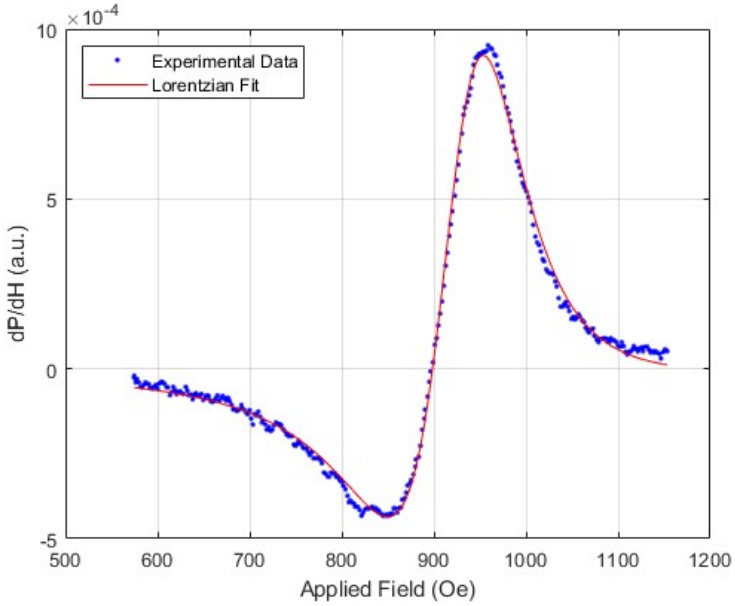

Figure 3.7: FMR response data for Ta/$Co_{25}Fe_{75}$ for a RF field of 13 GHz. The signal was applied at a power of 10 dBm, while the field was swept from 1271 to 1849 G. The data was fit to (4.1).

CHAPTER 4

SAMPLE GROWTH AND CHARACTERIZATION

4.1. Introduction

In this section, the effects of sample construction on the magnetic properties of $Co_{25}Fe_{75}$ films will be discussed. The method of deposition, as well as the results of characterization through the techniques introduced in the last section, will be presented. By modifying the environment around the $Co_{25}Fe_{75}$ layer, whether that be through the introduction of seed, capping, or spacer layers, the magnetic properties will also be modified. In particular, the damping parameter is especially sensitive to modifications of interface quality, as well as to the type neighboring material. It is possible to modify the damping parameter through control of these parameters, as will be demonstrated.

4.2. Sample Growth

Each sample was deposited through DC magnetron sputtering onto a Si wafer. Substrates were cleaned with acetone, isopropyl alcohol, and deionized water before being dried with dry N_2 in order to remove any dust or other contaminants adhered to the surface. The base pressure was better than 5×10^{-7}Torr for each deposition. The samples were sputtered at 5 mTorr Ar sputtering pressure, with 50 W DC power supplied to the target. This pressure was chosen in order to shift the energy distribution of sputtered material impinging on the substrate to lower energies, reducing diffusion between layers and resulting in cleaner interfaces. Deposition rates were calibrated through XRR. The sample mount was held at a fixed height for each deposition and the substrate was not heated during the deposition.

A set of 5 samples were grown to be measured with VSM and FMR, each with a layer of $Co_{25}Fe_{75}$. The target used during deposition was a stoichiometric alloy target (3:1 Fe to Co atomic ratio). A layer of $Co_{25}Fe_{75}$ was grown on bare Si to serve as a reference; the sample has a layer of natural oxides of Co and Fe, as both metals readily oxidize in air. A sample with a Ta seed layer was grown to improve adhesion of the $Co_{25}Fe_{75}$ layer and reduce surface roughness. This sample also has a layer of natural oxides on top. In order to prevent this, another sample with both a Ta seed and capping layer was grown. A sample with a Ta seed layer and a Pt capping layer was grown to compare to future works using Pt to induce interfacial DMI. The Ta seed and capping layers were grown at a nominal thickness of 3 nm. The Pt capping layer was 5 nm thick. A final sample was grown with 3 nm Cu spacer layers between the Ta layers and the $Co_{25}Fe_{75}$ layer. This was done to prevent contribution to damping from the magnetic proximity effect. For each sample, nominal layer thicknesses are reported in Table 4.2. The layer thicknesses were determined through the calibration of the deposition rate through XRR measurements.

4.3. XRR Measurements

To accurately determine deposition rates, samples were grown for each Ta, $Co_{25}Fe_{75}$, Pt, and Cu with timed depositions. The targets used were 0.25”, 0.125”, 0.125”, and 0.25” thick respectively. 15, 30, and 45 second depositions were carried out at 5 mTorr for each target. Layer thicknesses were then measured using XRR and linear regression was used to determine deposition rates. This fit is then used to determine deposition times for each sample measured with VSM and FMR. The XRR measurements also determine the density and roughness of each layer. It was found that $Co_{25}Fe_{75}$ grown on a Ta seed layer had a density on average of 6.3 ± 0.1

g/cm^3, and a roughness of 0.341 ± 0.004 nm. When the Cu spacer is inserted, $Co_{25}Fe_{75}$ had a density of 7.08 ± 0.02 g/cm^3 and a roughness of 1.81 ± 0.09 nm.

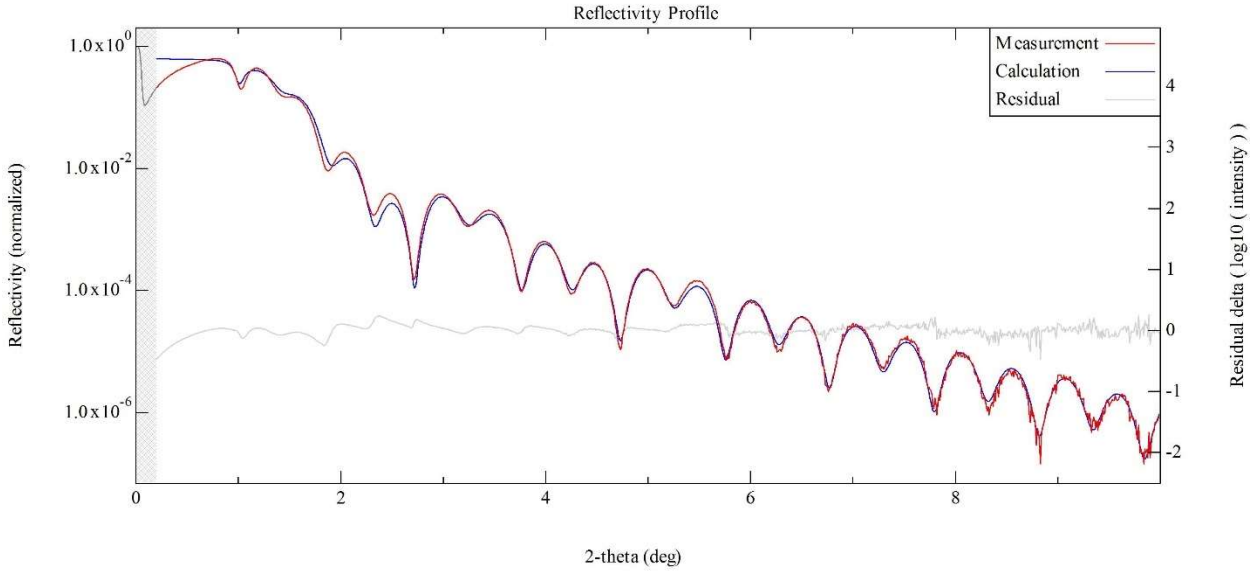

Figure 4.1: Reflectivity profile for Ta/$Co_{25}Fe_{75}$/Pt, 3/10/5 nm layer thicknesses, grown on Si. Each layer was deposited at 5 mTorr sputtering pressure. The XRR measurement was carried out over 28 minutes.

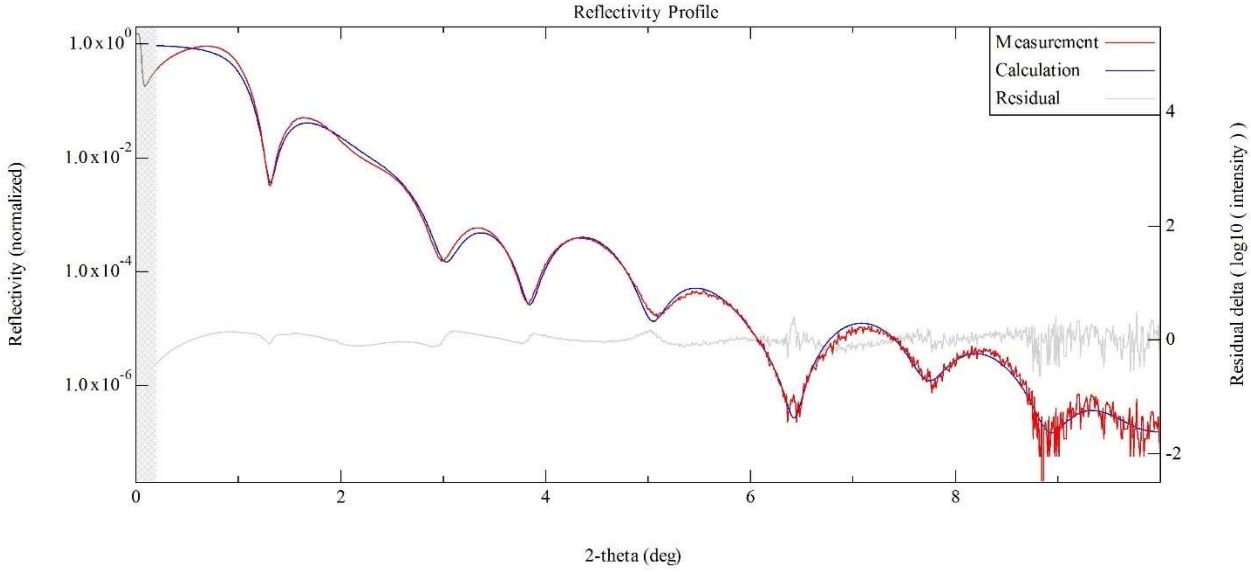

Figure 4.2: Reflectivity profile for Ta/$Co_{25}Fe_{75}$/Ta, 3/10/3 nm layer thicknesses, grown on Si. Each layer was deposited at 5 mTorr sputtering pressure. There are clear fringes present up to 10 degrees, indicating interfaces of low roughness.

4.4. VSM Measurements

Each sample was measured using VSM in order to determine the saturation magnetization M_s, with hysteresis loops shown in Figure 4.3. The samples were measured in the in-plane configuration, as to best match the configuration of the FMR measurements. A reference measurement was taken directly after each measurement, using a piece of the wafer used as a substrate for each sample, and the same sample rod and tape. The reference measurement was used to remove and signal from the substrate, as well as any Fe-containing dust adhered to the tape. The dimensions of the sample were measured using a microscope in order to calculate the volume of the sample. The signal was extracted according to (3.1), as discussed previously. The saturated regions were fit using linear regression, and the y-intercepts used to calculate M_s. The M_s values can be found in Table 4.1.

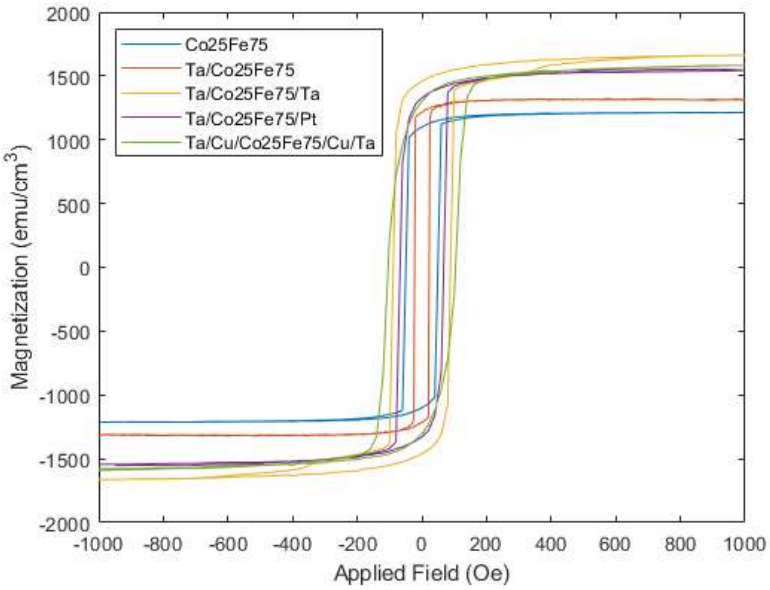

Figure 4.3: Hysteresis measurements made for each sample. Measurements were made by VSM, in the in-plane configuration. A reference scan was made with the same sample rod, tape, and a piece of the same wafer in order to remove their contribution from the signal. The signal was scaled by the volume of the magnetic layer in the sample. The linear portion of the loop, after saturation, was fit via linear regression and the y-intercept was used to find M_s.

4.5. FMR Measurements

To determine the damping parameter for each sample, FMR measurements were performed. The samples were measured in the in-plane configuration, with the microwave field held at a fixed frequency. Measurements were taken in the Ku band, from 12 – 18 GHz. As lock-in detection was used, the response data takes the form of the derivative of a Lorentzian. The data is thus fit to the derivative of (2.29),

$$\frac{dP}{dH} = a + bH - \frac{16c\cos(\theta)\sqrt{3}H_{pp}\left(H - H_{fmr}\right) + 4c\,sin(\theta)\left[3H_{pp}^2 - 4\left(H - H_{fmr}\right)^2\right]}{\pi\left[4\left(H - H_{fmr}\right)^2 + 3H_{pp}^2\right]^2} \quad (4.1)$$

where a, b, c, H_{fmr}, and H_{pp} are free parameters in the fitting, accounting for constant offset, linear drift in measurement, amplitude of response, resonant field respectively, and peak-to-peak linewidth.

H_{fmr} is used to fit to the Kittel equation for a thin film with uniaxial anisotropy, (2.19), where f is the microwave frequency in G, γ is the gyromagnetic ratio in GHz/Oe, M_s is the saturation magnetization in emu/cm^3 determined by VSM, and K is the uniaxial anisotropy energy density in erg/cm^3. The results are summarized in Table 4.1. The linewidth data, shown in Figure 4.5, was fit to (3.2), with α and ΔH_0 reported for each sample in Table 4.2.

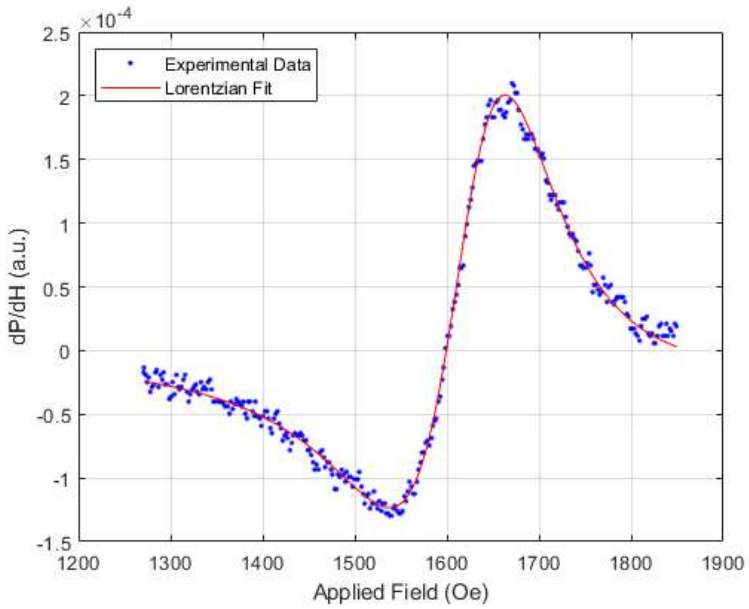

Figure 4.4: FMR response data (blue) for Ta/$Co_{25}Fe_{75}$ for a RF field of 18 GHz, with fit to equation (3.1), (red).

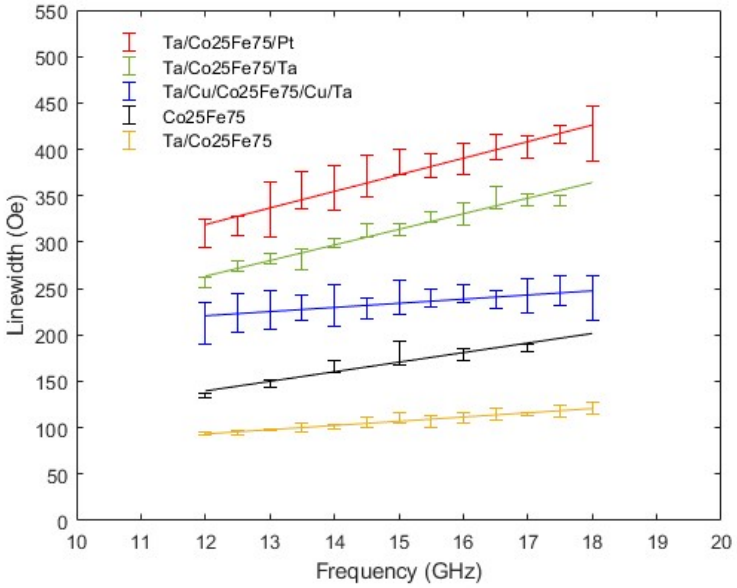

Figure 4.5: FMR resonant field linewidth versus frequency, where the points and error bars show the measured linewidths and associated uncertainties, and the solid lines show the fits to equation (2.2). Measurements were made in the in-plane configuration.

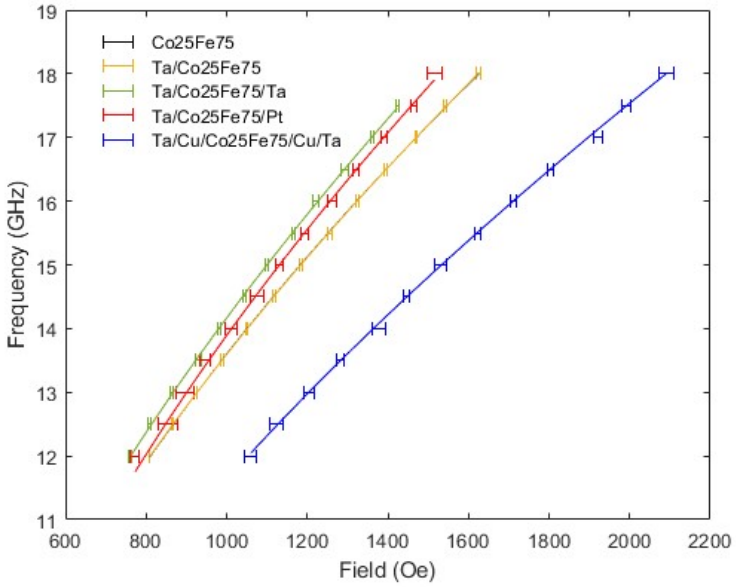

Figure 4.6: The FMR resonant frequency data were fit using the Kittel equation for thin films with in-plane anisotropy. Error bars are included for the data points, and the lines show the fits.

Table 4.1: Summary of the $4\pi M_s$ values for each sample obtained from the VSM measurements, as well as, from fitting the FMR resonant field data to the Kittel equation, (2.19), for thin films with in-plane anisotropy. The uniaxial anisotropy constant K was also obtained from the fits to the FMR data. The samples are labeled with the first layer on the left (e.g., Ta/$Co_{25}Fe_{75}$ corresponds to Si/Ta/$Co_{25}Fe_{75}$). Ta/Cu/$Co_{25}Fe_{75}$/Cu/Ta will be referred to as Ta/Cu/ $Co_{25}Fe_{75}$ for simplicity. The gyromagnetic ratio was set to $\frac{|\gamma|}{2\pi} = 2.95 \frac{MHz}{Oe}$, the value previously reported for Co25Fe75 [49], for the FMR fits.

Sample	Layer Thicknesses (nm)	4πMs, VSM (G)	4πMs, FMR (G)	K (Merg/cm^3)
$Co_{25}Fe_{75}$	[10]	15100 ± 400	27200 ± 800	-2.6 ± 0.4
Ta/$Co_{25}Fe_{75}$	[3/10]	15700 ± 300	23200 ± 100	-1.37 ± 0.07
Ta/$Co_{25}Fe_{75}$/Ta	[3/10/3]	18500 ± 300	26000 ± 500	-1.8 ± 0.2
Ta/$Co_{25}Fe_{75}$/Pt	[3/10/5]	17400 ± 300	25700 ± 500	-2.1 ± 0.3
Ta/Cu/$Co_{25}Fe_{75}$/Cu/Ta	[3/3/10/3/3]	17500 ± 400	17000 ± 300	-2.11 ± 0.16

Table 4.2: Summary of linear fit of the FMR linewidths. The damping parameters are reported, along with the inhomogeneous line broadening.

Sample	α (-)	ΔH_0 (Oe)
$Co_{25}Fe_{75}$	0.014 ± 0.003	20 ± 60
$Ta/Co_{25}Fe_{75}$	0.0064 ± 0.0004	39 ± 8
$Ta/Co_{25}Fe_{75}/Ta$	0.024 ± 0.002	60 ± 30
$Ta/Co_{25}Fe_{75}/Pt$	0.025 ± 0.002	100 ± 40
$Ta/Cu/Co_{25}Fe_{75}/Cu/Ta$	0.006 ± 0.001	170 ± 20

4.6. Saturation Magnetization

The saturation magnetizations obtained from the two different measurement methods differ significantly (Table 4.1). The VSM measurements give reduced saturation magnetizations when compared to FMR measurements for two reasons. The VSM measures the total magnetic moment of the sample and these are divided by the sample volume to obtain the M_s values reported in Table 4.1. The nominal thicknesses reported in Table 4.1 were used to calculate the sample volume. The actual thicknesses of the magnetic layers are, however, likely smaller than the nominal values due to oxidization of the uncapped samples and dead layers from interfacial effects such as diffusion of material between layers. A reduction of the volume from the volume calculated by the deposition rate will results in an apparently smaller M_s value, which is what is seen in Table 4.1 where the M_s values measured by VSM are smaller than those measured by FMR. In contrast, the FMR measurements do not depend on knowing the volume of magnetic material and thus do not require correcting for oxidation or dead layers. In each sample, a small perpendicular anisotropy field is present, resulting from the broken symmetry of the interfaces in each sample. The anisotropy constants reported in Table 4.1 are small and are similar to the values reported by Schoen *et al.* (Figure 4(c) in [50]). To understand the scale, it is helpful to

convert the anisotropy constants to effective fields, $H_k = \frac{2K}{M_s}$. For the Ta/$Co_{25}Fe_{75}$, $H_k = 108\ Oe$, which is small compared to the ~kOe applied magnetic field.

The M_s values determined via VSM, reported in Table 4.1, are lower than those reported for $Co_{25}Fe_{75}$ (24000 Oe) by Schoen *et al* [50]. This discrepancy arises from differences in the method used to determine of the volume of magnetic material. For the uncapped samples, exposure to ambient oxygen forms an oxide layer, reducing the volume of the magnetic layer. The thickness at time of deposition was used to calculate M_s from the VSM data, resulting in an artificial reduction in M_s. XRR measurements would be required to determine the thickness of the remaining $Co_{25}Fe_{75}$. Layers of reduced magnetization, or dead layers, also need to be considered for each sample. During deposition, the sputtered material arriving at the sample can diffuse into the previously deposited layers, with increased energy of impinging material resulting in increased diffusion. The power supplied to the sputtering target during deposition, the distance from the target to the sample, and the sputtering pressure all affect the energy profile of the sputtered material, and thus necessarily affect the amount of diffusion between layers. Changes in diffusion would change the thickness of the dead layers, as the depth of penetration of material into the magnetic layer would be different.

A method for extracting the true M_s, as well as the thickness of the dead layers, was employed by Schoen *et al*. [50]. They use a thickness series of $Co_{25}Fe_{75}$, measured via FMR, to determine the true M_s, as well as the thickness of the dead layers. To do so, M_s is determined by FMR, and linear regression is performed on M_s vs. $1/t$, where t is the thickness of the sample. The *y*-intercept corresponds to the case of infinite thickness, where any interfacial effects vanish, giving M_s. The *x*-intercept gives the thicknesses of the dead layers. Schoen *et al*. report a 0.7 ± 0.3 nm dead layer, which is used to adjust the volume of magnetic material. This reduction in

volume results in a larger measured M_s. For a 10 nm layer, accounting for a 0.7-nm thick dead layer would increase the apparent M_s measured by 14%. For instance, a sample with a measured M_s of 17500 G would be increased to 19950 G after correcting for the dead layer. The samples in Table 4.1 likely have dead layers of comparable thickness. To determine the thickness of the dead layers accurately, a thickness series would need to be grown since the dead layer thicknesses are expected to vary depending on the deposition conditions.

The M_s values were also obtained by fitting the resonant field data to the Kittel equation, (2.19), while fixing the gyromagnetic ratio at $\frac{|\gamma|}{2\pi} = 2.95\ MHz/Oe$, the value determined by Schoen *et al.* [49] for $Co_{25}Fe_{75}$. The M_s and K values obtained from the fits are summarized in Table 4.1. The M_s values obtained from the FMR fits are larger than the VSM values, but are roughly in line with, or marginally higher than, the reported value for M_s (2.41 ± 0.08 G, obtained from Figure 3(c) in [10]). The differences in these M_s values can be attributed to the choice of $\frac{|\gamma|}{2\pi}$ used in the fitting. For instance, a small increase in $\frac{|\gamma|}{2\pi}$, from 2.95 to 3.05 MHz/Oe is sufficient to reduce the M_s fit value to 2.54 ± 0.07 for the $Co_{25}Fe_{75}$ sample, which is in agreement with the reported value. The gyromagnetic ratio, given by

$$\frac{|\gamma|}{2\pi} = \frac{g\mu_B}{h} \tag{4.2}$$

in which g is the Landé g-factor, μ_B is the Bohr magneton, and h is Planck's constant, depends linearly to the g-factor. Approximately 2 for a free electron, g can be raised through orbital contributions to the magnetic moment. Spin-orbit coupling between layers can cause an enhanced orbital component of the moment in the interfacial region due to modification of the electronic structure of atoms in this region [51]. There is expected to be strong spin-orbit coupling between the Ta and Pt layers interfaced with $Co_{25}Fe_{75}$, which would explain the

enhanced g-factor in these samples. Likewise, hybridization of Co and Fe valence orbitals with the valence orbitals of O present in the oxide layer formed on the uncapped samples could be a source for an increase orbital moment [52]. The interfacial regions of these samples represent a significant portion of the 10 nm thickness, hence interfacial effects can affect the magnetic behavior of the samples.

4.7. Damping

The addition of different layers modifies the damping in each sample, as shown in Table 4.2. Using a seed layer of Ta resulted in a reduction in damping of 0.008 ± 0.003 (from 0.014 ± 0.003 to 0.0064 ± 0.0004) as compared to $Co_{25}Fe_{75}$. As shown by XRR, the seed layer promoted a smoother $Co_{25}Fe_{75}$ layer, with low RMS roughness (0.341 ± 0.003 nm). A smoother layer is expected to lead to reductions in the damping contributions from two-magnon scattering, in which the uniform FMR mode is scattered into two magnons of equal and opposite wavevectors [53]. Approaching the ideal planar boundary reduces these effects. The measured value of α for the Ta/ $Co_{25}Fe_{75}$ sample is 0.0064 ± 0.0004. This value is in line with reported results (0.005 in Weber *et al.* [11]).

The addition of the Pt and Ta layers resulted in enhanced damping, due to contributions from the magnetic proximity effect (MPE), as well as, spin pumping. Magnetic proximity effects often occur when a nonmagnetic heavy metal layer is magnetized due to interactions with an adjacent ferromagnetic layer, where the thickness of the layer magnetized through the proximity effect is on the order of single nanometer [54]. The presence of the MPE results in a contribution to the damping reportedly on the order of 10^{-3} in Yttrium Iron Garnet (YIG) capped with Pt [55]. In the Ta/ $Co_{25}Fe_{75}$/Ta and Ta/ $Co_{25}Fe_{75}$/Pt samples, the addition of both the capping and seed layers resulted in an increase in alpha to 0.0235 ± 0.0016 for the Ta-capped sample, and 0.0250

± 0.0018 for the Pt-capped sample. These values are both considerably larger than the damping value obtained for the Ta/ $Co_{25}Fe_{75}$ sample of 0.0064 ± 0.0004 . The increase was an order of magnitude greater than that reported for YIG capped with Pt. The damping parameters are the same within uncertainty for the two capping layers considered.

The MPE contribution to damping also displays a critical thickness behavior, where below the critical thickness of HM capping layer [55], the contribution to the damping is negligible. For Ta/ $Co_{25}Fe_{75}$, the MPE does not contribute at the same level, if at all, as observed in the samples with the capping layers. For this reason, it is proposed that the seed layer was thinner than the critical thickness for the MPE to contribute. In addition, the interface between the seed and magnetic layers is not identical to the magnetic and capping layers. Seed layers are commonly used to promote smooth growth of the magnetic layer and are typically about 3 nm in thickness, as the seed layers are in this work.

In order to minimize the MPE damping contribution, Cu spacers were inserted between the $Co_{25}Fe_{75}$ layer and the seed and capping layers. By inserting the Cu spacer, the direct interface between the Ta seed layer and $Co_{25}Fe_{75}$ layer is disrupted, preventing the contribution from the MPE. The addition of the Cu spacers resulted in a low damping, but in increased inhomogeneous line broadening. This is due to the Cu spacer layers growing roughly on the Ta, as demonstrated through XRR measurement. The roughness of the Cu layer consequently increased the roughness of the $Co_{25}Fe_{75}$ layer grown on it, from 0.341 nm to 1.81 nm roughness as determined by XRR. Increased roughness of the $Co_{25}Fe_{75}$ is expected to increase two-magnon scattering contributions to the damping, and it is also expected to lead to increased inhomogeneous line broadening, resulting in a larger ΔH_0 (170 ± 20 for Ta/Cu/ $Co_{25}Fe_{75}$ compared to 60 ± 30 for Ta/ $Co_{25}Fe_{75}$/Ta).

For some of the samples, an additional contribution to the damping comes in the form of spin pumping. The contribution, α_{sp}, is described by

$$\alpha_{sp} = \frac{g\mu_B}{4\pi M_s} g_{\uparrow\downarrow} \frac{1}{d} \tag{4.3}$$

where g is the Landé g-factor, μ_B is the Bohr magneton, M_s is the saturation magnetization, $g_{\uparrow\downarrow}$ is the spin mixing conductance, and d is the thickness of the magnetic layer [55]. Spin pumping is expected to be seen when the magnetic layer is adjacent to any metal, thus it is expected to be seen in the Ta/ $Co_{25}Fe_{75}$, Ta/ $Co_{25}Fe_{75}$/Ta, Ta/ $Co_{25}Fe_{75}$/Pt, and Ta/Cu/ $Co_{25}Fe_{75}$ samples [56]. The samples with more than one adjacent metallic layer (Ta/ $Co_{25}Fe_{75}$/Ta, Ta/ $Co_{25}Fe_{75}$/Pt, and Ta/Cu/ $Co_{25}Fe_{75}$) should have greater contributions from spin pumping than Ta/ $Co_{25}Fe_{75}$. The spin mixing conductance for $Co_{25}Fe_{75}$, as reported in [49], is approximately unity.

At the interface of Ta, or Pt, layers with the $Co_{25}Fe_{75}$, the spin pumping into the non-magnetic layers provides a significant source of damping, on the order of 10^{-3} [49]. The direct interface between the ferromagnetic and non-magnetic layers in these samples allows the spin pumping process to proceed directly. In the sample with Cu spacer layers, the Cu layer lies between the Ta and the $Co_{25}Fe_{75}$. Cu has a spin diffusion length of 500 nm at room temperature [57], allowing the spin pumping into the Ta layer to proceed uninhibited, as the thickness of the layer (3 nm) is much less than the spin diffusion length.

Comparing our results to literature, the lowest damping values obtained in this work, which were for Ta/Cu/ $Co_{25}Fe_{75}$ (0.0063 ± 0.0011) and Ta/ $Co_{25}Fe_{75}$ (0.0064 ± 0.0004), were in agreement with results from Weber *et al.* [11] ($\alpha = 0.005$, extrapolating from Figure 2 in [11]) . They are about a factor of 3 larger than results from Edwards *et al.* [58] ($\alpha < 0.0020$) and Schoen *et al.* [10] ($\alpha = 0.0021 \pm 0.0001$). As film quality impacts the damping parameter, mainly through the suppression or enhancement of two-magnon scattering, the poor quality

growth of the Cu spacer layers in Ta/Cu/ $Co_{25}Fe_{75}$ that lead to higher film roughness is the likely cause of the enhanced damping parameter. Lowering the power supplied to the Cu target during deposition, as well as raising the sputtering pressure, are possible avenues to promote a higher quality film by shifting the energy profile of sputtered Cu to lower energies to reduce nucleation rates in the film [59]. Reduced nucleation rates during growth result in smaller grains in the film, which reduce the roughness of the film.

4.8. Conclusion

In summary, the damping in $Co_{25}Fe_{75}$ films depend strongly on the construction of the sample. A Ta seed layer effectively reduces the damping by promoting the growth of a smooth $Co_{25}Fe_{75}$ layer. A capping layer is used to prevent oxidation of the magnetic layer, which would create a dead region near the surface that is no longer magnetic. Directly interfacing the magnetic layer with both a seed and capping layer of heavy metals provides an increase in damping on the order of 10^{-2} due to the magnetic proximity effect. The insertion of Cu spacers between the seed and capping layer prevent this contribution to the damping, but also increases the roughness of the $Co_{25}Fe_{75}$ layer, causing a corresponding increase in inhomogeneous line broadening of the FMR spectrum. The lowest damping parameters of approximately 0.006, obtained from the Ta/$Co_{25}Fe_{75}$ and Ta/Cu/$Co_{25}Fe_{75}$/Cu/Ta samples, are in agreement with some published results, but still above the lowest reported values of 0.0020. Fine tuning of the growth of the Cu spacers to reduce the roughness of the $Co_{25}Fe_{75}$ grown on top would be the next step to reduce the damping further. A thickness series for the Cu spacers could also help determine the ideal thickness of the spacer layer after this.

BIBLIOGRAPHY

[1] N. Nishimura, T. Hirai, A. Koganei, T. Ikeda, K. Okano, Y. Sekiguchi, Y. Osada, Magnetic tunnel junction device with perpendicular magnetization films for high-density magnetic random access memory, J. Appl. Phys. 91 (2002) 5246–5249. https://doi.org/10.1063/1.1459605.

[2] S.S.P. Parkin, K.P. Roche, M.G. Samant, P.M. Rice, R.B. Beyers, R.E. Scheuerlein, E.J. O'Sullivan, S.L. Brown, J. Bucchigano, D.W. Abraham, Y. Lu, M. Rooks, P.L. Trouilloud, R.A. Wanner, W.J. Gallagher, Exchange-biased magnetic tunnel junctions and application to nonvolatile magnetic random access memory (invited), J. Appl. Phys. 85 (1999) 5828–5833. https://doi.org/10.1063/1.369932.

[3] I.M.P. Doyle, G. Dale, H. Choi, B. City, (12) UnIted States Patent, 2 (2012). https://doi.org/10.1126/science.Liquids.

[4] S. Kaka, M.R. Pufall, W.H. Rippard, T.J. Silva, S.E. Russek, J.A. Katine, Mutual phase-locking of microwave spin torque nano-oscillators, Nature. 437 (2005) 389–392. https://doi.org/10.1038/nature04035.

[5] D. Houssameddine, U. Ebels, B. Delaët, B. Rodmacq, I. Firastrau, F. Ponthenier, M. Brunet, C. Thirion, J.P. Michel, L. Prejbeanu-Buda, M.C. Cyrille, O. Redon, B. Dieny, Spin-torque oscillator using a perpendicular polarizer and a planar free layer, Nat. Mater. 6 (2007) 447–453. https://doi.org/10.1038/nmat1905.

[6] S. Bonetti, P. Muduli, F. Mancoff, J. Åkerman, Spin torque oscillator frequency versus magnetic field angle: The prospect of operation beyond 65 GHz, Appl. Phys. Lett. 94 (2009) 92–95. https://doi.org/10.1063/1.3097238.

[7] S. Jain, A. Ranjan, K. Roy, A. Raghunathan, Computing in Memory with Spin-Transfer Torque Magnetic RAM, IEEE Trans. Very Large Scale Integr. Syst. 26 (2017) 470–483. https://doi.org/10.1109/TVLSI.2017.2776954.

[8] J. Li, P. Ndai, A. Goel, S. Salahuddin, K. Roy, Design paradigm for robust spin-torque transfer magnetic RAM (STT MRAM) from circuit/architecture perspective, IEEE Trans. Very Large Scale Integr. Syst. 18 (2010) 1710–1723. https://doi.org/10.1109/TVLSI.2009.2027907.

[9] Z. Wang, H. Zhou, M. Wang, W. Cai, D. Zhu, J.O. Klein, W. Zhao, Proposal of Toggle Spin Torques Magnetic RAM for Ultrafast Computing, IEEE Electron Device Lett. 40 (2019) 726–729. https://doi.org/10.1109/LED.2019.2907063.

[10] M.A.W. Schoen, D. Thonig, M.L. Schneider, T.J. Silva, H.T. Nembach, O. Eriksson, O. Karis, J.M. Shaw, Ultra-low magnetic damping of a metallic ferromagnet, 12 (2016) 2–6. https://doi.org/10.1038/NPHYS3770.

[11] R. Weber, D.S. Han, I. Boventer, S. Jaiswal, R. Lebrun, G. Jakob, M. Kläui, Gilbert damping of CoFe-alloys, J. Phys. D. Appl. Phys. 52 (2019). https://doi.org/10.1088/1361-6463/ab2096.

[12] J.D. Jackson, R.F. Fox, Classical Electrodynamics, 3rd ed . , Am. J. Phys. 67 (1999) 841–842. https://doi.org/10.1119/1.19136.

[13] C. Kittel, On the theory of ferromagnetic resonance absorption, Phys. Rev. 73 (1948) 155–161. https://doi.org/10.1103/PhysRev.73.155.

[14] J.H. Moon, S.M. Seo, K.J. Lee, K.W. Kim, J. Ryu, H.W. Lee, R.D. McMichael, M.D. Stiles, Spin-wave propagation in the presence of interfacial Dzyaloshinskii-Moriya interaction, Phys. Rev. B. 88 (2013). https://doi.org/10.1103/PhysRevB.88.184404.

[15] T. Xagamiya, K. Yosida, AnisotropicSuperexchangeInteractionandWeak Ferromagnets, 1958.

[16] A. Thiaville, Y. Nakatani, J. Miltat, Y. Suzuki, Micromagnetic understanding of current-driven domain wall motion in patterned nanowires, Europhys. Lett. 69 (2005) 990–996. https://doi.org/10.1209/epl/i2004-10452-6.

[17] J. Iwasaki, M. Mochizuki, N. Nagaosa, Universal current-velocity relation of skyrmion motion in chiral magnets, Nat. Commun. 4 (2013). https://doi.org/10.1038/ncomms2442.

[18] L. LANDAU, E. LIFSHITZ, On the theory of the dispersion of magnetic permeability in ferromagnetic bodies, Perspect. Theor. Phys. 169 (1992) 51–65. https://doi.org/10.1016/b978-0-08-036364-6.50008-9.

[19] T.L. Gilbert, Classics in Magnetics A Phenomenological Theory of Damping in Ferromagnetic Materials, 40 (2004) 3443–3449.

[20] F. Bloch, Nuclear induction, Phys. Rev. 70 (1946) 460–474. https://doi.org/10.1103/PhysRev.70.460.

[21] V. Kambersky, C.E. Patton, Spin-wave relaxation and phenomenological damping in ferromagnetic resonance, Phys. Rev. B. 11 (1975) 2668–2672. https://doi.org/10.1103/PhysRevB.11.2668.

[22] V.L. Safonov, H.N. Bertram, Linear stochastic magnetization dynamics and microscopic relaxation mechanisms, J. Appl. Phys. 94 (2003) 529–538. https://doi.org/10.1063/1.1581349.

[23] B.K. Kuanr, R.E. Camley, Z. Celinski, Extrinsic contribution to Gilbert damping in sputtered NiFe films by ferromagnetic resonance, J. Magn. Magn. Mater. 286 (2005) 276–281. https://doi.org/10.1016/j.jmmm.2004.09.080.

[24] A.Y. Dobin, R.H. Victora, Surface roughness induced extrinsic damping in thin magnetic films, Phys. Rev. Lett. 92 (2004) 1–4. https://doi.org/10.1103/PhysRevLett.92.257204.

[25] R.D. McMichael, M.D. Stiles, P.J. Chen, W.F. Egelhoff, Ferromagnetic resonance linewidth in thin films coupled to NiO, J. Appl. Phys. 83 (1998) 7037–7039. https://doi.org/10.1063/1.367725.

[26] A.K. Srivastava, M.J. Hurben, M.A. Wittenauer, P. Kabos, C.E. Patton, R. Ramesh, P.C. Dorsey, D.B. Chrisey, Angle dependence of the ferromagnetic resonance linewidth and two magnon losses in pulsed laser deposited films of yttrium iron garnet, MnZn ferrite, and NiZn ferrite, J. Appl. Phys. 85 (1999) 7838–7848. https://doi.org/10.1063/1.370595.

[27] Y. Sun, H. Chang, M. Kabatek, Y.Y. Song, Z. Wang, M. Jantz, W. Schneider, M. Wu, E. Montoya, B. Kardasz, B. Heinrich, S.G.E. Te Velthuis, H. Schultheiss, A. Hoffmann, Damping in yttrium iron garnet nanoscale films capped by platinum, Phys. Rev. Lett. 111 (2013). https://doi.org/10.1103/PhysRevLett.111.106601.

[28] J. Smit, H.G. Beljers, Ferromagnetic Resonance Absorption in BaFe12O19, A Highly Anisotropic Crystal, (n.d.).

[29] R.F. Bunshah, C. V. Deshpandey, Plasma assisted physical vapor deposition processes: A review, J. Vac. Sci. Technol. A Vacuum, Surfaces, Film. 3 (1985) 553–560. https://doi.org/10.1116/1.572993.

[30] U. Helmersson, M. Lattemann, J. Bohlmark, A.P. Ehiasarian, J.T. Gudmundsson, Ionized physical vapor deposition (IPVD): A review of technology and applications, Thin Solid Films. 513 (2006) 1–24. https://doi.org/10.1016/j.tsf.2006.03.033.

[31] P.J. Kelly, R.D. Arnell, Magnetron sputtering: A review of recent developments and applications, Vacuum. 56 (2000) 159–172. https://doi.org/10.1016/S0042-

207X(99)00189-X.

[32] I. Safi, Recent aspects concerning DC reactive magnetron sputtering of thin films: A review, Surf. Coatings Technol. 127 (2000) 203–218. https://doi.org/10.1016/s0257-8972(00)00566-1.

[33] J. Singh, D.E. Wolfe, Nano and macro-structured component fabrication by electron beam-physical vapor deposition (EB-PVD), J. Mater. Sci. 40 (2005) 1–26. https://doi.org/10.1007/s10853-005-5682-5.

[34] M. Ohring, Materials Science of Thin Films: Deposition & Structure, Second Ed., 2002. https://doi.org/10.1128/AAC.03728-14.

[35] L. Nevot, B. Pardo, J. Corno, Characterization of X-UV multilayers by grazing incidence X-ray reflectometry, Rev. Phys. Appliquée. 23 (1988) 1675–1686. https://doi.org/10.1051/rphysap:0198800230100167500.

[36] D.B. Judd, Fresnel reflection of diffusely incident light, J. Res. Natl. Bur. Stand. (1934). 29 (1942) 329. https://doi.org/10.6028/jres.029.017.

[37] E. Chason, T.M. Mayer, Thin film and surface characterization by specular X-ray reflectivity, 1997. https://doi.org/10.1080/10408439708241258.

[38] A. Ulyanenkov, K. Omote, J. Harada, The genetic algorithm : re " nement of X-ray re # ectivity data from multilayers and thin " lms, 283 (2000) 237–241.

[39] S. Foner, Versatile and sensitive vibrating-sample magnetometer, Rev. Sci. Instrum. 30 (1959) 548–557. https://doi.org/10.1063/1.1716679.

[40] M.S. Lubell, A.S. Venturino, Vibrating sample magnetometer, Rev. Sci. Instrum. 31 (1960) 207–208. https://doi.org/10.1063/1.1716932.

[41] Microsense.net/products-vsm.htm, EZ VSM HF 11 has a sensitivity of 125 nemu., n.d.

[42] M.A. Garcia, E. Fernandez Pinel, J. De La Venta, A. Quesada, V. Bouzas, J.F. Fernández, J.J. Romero, M.S. Martín González, J.L. Costa-Krämer, Sources of experimental errors in the observation of nanoscale magnetism, J. Appl. Phys. 105 (2009). https://doi.org/10.1063/1.3060808.

[43] J.H.E. Griffiths, Anomalous high-frequency resistance of ferromagnetic metals [13], Nature. 158 (1946) 670–671. https://doi.org/10.1038/158670a0.

[44] C.J. Brower, C.E. Patton, Determination of anisotropy field in polycrystalline lithium ferrites from FMR linewidths, J. Appl. Phys. 53 (1982) 2104–2106. https://doi.org/10.1063/1.330712.

[45] B. Heinrich, J.F. Cochran, M. Kowalewski, J. Kirschner, Z. Celinski, A.S. Arrott, K. Myrtle, Magnetic anisotropies and exchange coupling in ultrathin fcc Co(001) structures, Phys. Rev. B. 44 (1991) 9348–9361. https://doi.org/10.1103/PhysRevB.44.9348.

[46] B. Heinrich, Y. Tserkovnyak, G. Woltersdorf, A. Brataas, R. Urban, G.E.W. Bauer, Dynamic Exchange Coupling in Magnetic Bilayers, Phys. Rev. Lett. 90 (2003) 4. https://doi.org/10.1103/PhysRevLett.90.187601.

[47] M. Oogane, T. Wakitani, S. Yakata, R. Yilgin, Y. Ando, A. Sakuma, T. Miyazaki, Magnetic damping in ferromagnetic thin films, Japanese J. Appl. Physics, Part 1 Regul. Pap. Short Notes Rev. Pap. 45 (2006) 3889–3891. https://doi.org/10.1143/JJAP.45.3889.

[48] O. Yaln, ed., Ferromagnetic Resonance - Theory and Applications, InTech, 2013. https://doi.org/10.5772/50583.

[49] M.A.W. Schoen, J. Lucassen, H.T. Nembach, B. Koopmans, T.J. Silva, C.H. Back, J.M. Shaw, Magnetic properties in ultra-thin 3d transition metal alloys II: Experimental verification of quantitative theories of damping and spin-pumping, n.d.

[50] M.A.W. Schoen, J. Lucassen, H.T. Nembach, T.J. Silva, B. Koopmans, C.H. Back, J.M. Shaw, Magnetic properties of ultrathin 3 d transition-metal binary alloys . I . Spin and orbital moments , anisotropy , and confirmation of Slater-Pauling behavior, 134410 (2017) 1–9. https://doi.org/10.1103/PhysRevB.95.134410.

[51] J. Okabayashi, Y. Miura, H. Munekata, Anatomy of interfacial spin-orbit coupling in Co/Pd multilayers using X-ray magnetic circular dichroism and first-principles calculations, Sci. Rep. 8 (2018) 1–9. https://doi.org/10.1038/s41598-018-26195-w.

[52] S.M. Ahn, G.S.D. Beach, Crossover between in-plane and perpendicular anisotropy in Ta/Co xFe100-x/MgO films as a function of Co composition, J. Appl. Phys. 113 (2013) 2011–2014. https://doi.org/10.1063/1.4799779.

[53] D.J. Twisselmann, R.D. McMichael, Intrinsic damping and intentional ferromagnetic resonance broadening in thin permalloy films, J. Appl. Phys. 93 (2003) 6903–6905. https://doi.org/10.1063/1.1543884.

[54] C. Klewe, T. Kuschel, J.M. Schmalhorst, F. Bertram, O. Kuschel, J. Wollschläger, J. Strempfer, M. Meinert, G. Reiss, Static magnetic proximity effect in Pt/ Ni1-x Fex bilayers investigated by x-ray resonant magnetic reflectivity, Phys. Rev. B. 93 (2016) 1–8. https://doi.org/10.1103/PhysRevB.93.214440.

[55] Y. Sun, H. Chang, M. Kabatek, Y. Song, Z. Wang, M. Jantz, W. Schneider, M. Wu, S.G.E. Velthuis, H. Schultheiss, A. Hoffmann, Damping in Yttrium Iron Garnet Nanoscale Films Capped by Platinum, 106601 (2013) 1–5. https://doi.org/10.1103/PhysRevLett.111.106601.

[56] Y. Tserkovnyak, A. Brataas, G.E.W. Bauer, Spin pumping and magnetization dynamics in metallic multilayers, Phys. Rev. B - Condens. Matter Mater. Phys. 66 (2002) 1–10.

https://doi.org/10.1103/PhysRevB.66.224403.

[57] T. Kimura, J. Hamrle, Y. Otani, Estimation of spin-diffusion length from the magnitude of spin-current absorption: Multiterminal ferromagnetic/nonferromagnetic hybrid structures, Phys. Rev. B - Condens. Matter Mater. Phys. 72 (2005) 1–6. https://doi.org/10.1103/PhysRevB.72.014461.

[58] E.R.J. Edwards, H.T. Nembach, J.M. Shaw, Co25Fe75 Thin Films with Ultralow Total Damping of Ferromagnetic Resonance, Phys. Rev. Appl. 11 (2019) 1. https://doi.org/10.1103/PhysRevApplied.11.054036.

[59] M.T. Le, Y.U. Sohn, J.W. Lim, G.S. Choi, Effect of sputtering power on the nucleation and growth of Cu films deposited by magnetron sputtering, Mater. Trans. 51 (2010) 116–120. https://doi.org/10.2320/matertrans.M2009183.